Geochemistry, Geophysics, Geosystems

RESEARCH ARTICLE
10.1029/2020GC009377

Key Points:

- Mantle annealing under certain conditions induces discontinuous recrystallization altering its microstructure
- Xenoliths from Wyoming craton show annealing microstructures similar to experiments of deformation followed by annealing
- Conditions of high stresses and temperatures induce static recrystallization with calculated timescale of a week to a year

Supporting Information:

- Supporting Information S1
- Movie S1

Correspondence to:
Y. Boneh,
bonehyuv@bgu.ac.il

Citation:
Boneh, Y., Chin, E. J., Chilson-Parks, B. H., Saal, A. E., Hauri, E. H., Hearn, B. C., & Hirth, G. (2021). Microstructural shift due to post-deformation annealing in the upper mantle. *Geochemistry, Geophysics, Geosystems*, *22*, e2020GC009377. https://doi.org/10.1029/2020GC009377

Received 14 AUG 2020
Accepted 16 DEC 2020

Microstructural Shift due to Post-Deformation Annealing in the Upper Mantle

Yuval Boneh[1,2], Emily J. Chin[3], Benjamin H. Chilson-Parks[1,4], Alberto E. Saal[1], Erik H. Hauri[5], B. Carter Hearn, Jr.[6], and Greg Hirth[1]

[1]Department of Earth, Environmental, and Planetary Sciences, Brown University, Providence, RI, USA, [2]Department of Earth and Environmental Sciences, Ben-Gurion University of the Negev, Be'er Sheva, Israel, [3]Geosciences Research Division, Scripps Institution of Oceanography, University of California San Diego, La Jolla, CA, USA, [4]Department of Geosciences, University of Connecticut, Storrs, CT, USA, [5]Department of Terrestrial Magnetism, Carnegie Institution for Science, Washington, DC, USA, [6]McLean, VA, USA

Abstract Syntectonic microstructural evolution is a well-known phenomenon in the mantle and lower crust associated with two main processes: grain size reduction through dynamic recrystallization and development of crystallographic preferred orientation (CPO). However, the effects of annealing via static recrystallization on grain size and CPO have been largely overlooked. We investigated mantle annealing by analyzing a suite of kimberlite-hosted garnet peridotite xenoliths from the Wyoming Craton. We focus on five xenoliths that show microstructures reflecting different degrees of recrystallization, with annealed grains characterized by distinctive faceted boundaries crosscutting surrounding, nonfaceted matrix grains. These textures are indicative of discontinuous static recrystallization (DiSRX). Electron backscatter diffraction analysis further demonstrates a ~10°–20° misorientation between DiSRXed grains and the matrix grains, resulting in an overall weaker CPO. These characteristics are remarkably similar to microstructures observed in samples that were annealed after deformation in the laboratory. Measurements of the thermal conditions and water contents associated with the last equilibration of the xenoliths suggests that high homologous temperatures ($T/T_m > 0.9$) are necessary to induce DiSRX. We postulate that annealing through DiSRX occurs under high temperatures after a short episode of intense deformation (years to hundreds of years) with timescales for annealing estimated as weeks to years, significantly slower than the timescale of hours expected for a kimberlitic magma ascent. We conclude that microstructural transformation due to DiSRX will occur during transient heating events associated with mantle upwelling, plumes, and lithospheric thinning.

Plain Language Summary Our knowledge of large-scale processes in the mantle requires the understanding of mantle microstructures and their evolution under different conditions. During deformation and flow, grain size often decreases and rocks develop a preferred orientation of their crystallographic structure; features that correlate with the flow stress and strain magnitudes. However, there is a lack of knowledge regarding how the microstructure (e.g., grain size and crystallographic orientation) may change when deformation ceases—which promotes annealing. We investigate microstructures of mantle samples (xenoliths brought to the surface by volcanism) that experienced annealing. The partially annealed samples display evidence for a process in which some grains grow at the expense of others, resulting in a significant change to the preexisting microstructure. A comparison of the naturally annealed samples to samples that were deformed and then annealed in the laboratory reveals remarkable similarities. We discuss our results in the context of the timescales and conditions necessary to induce the relevant annealing mechanism, and demonstrate that a shift in microstructure occurs when deformed mantle undergoes a stage of heating.

1. Introduction

Upper mantle dynamics and kinematics are affected by the microstructures of the mantle, which evolve in response to changes in applied stress and the ambient thermochemical conditions. In particular, the grain size and crystallographic preferred orientation (CPO) of olivine, the most abundant mantle mineral, are considered to control much of the upper mantle's rheological, elastic, and electromagnetic properties (Christensen, 1984; Hirth & Kohlstedt, 2003). Grain size reduction through dynamic recrystallization and the formation of CPO are two major microstructural processes associated with deformation through a dislocation-mediated mechanism in the upper mantle. Grain size evolution through dynamic recrystallization occurs when new grains are formed by bulging of migrating grain boundaries or by increasing rotation of subgrains (Drury & Urai, 1990; Urai et al., 1986). Importantly, the sizes of dynamically recrystallized olivine grains are shown to reflect the applied stresses (Gueguen & Darot, 1980; Twiss, 1977; Van der Wal et al., 1993) and are often used as a piezometer to constrain the stresses during deformation of the mantle. The formation of CPO, formed by systematic rotation of crystal lattices during deformation, is used to infer strain and mantle flow kinematics from the anisotropy of seismic waves (Long & Becker, 2010; Skemer & Hansen, 2016). Characterization of these microstructure elements is also used to infer the dominant deformation mechanism (e.g., Warren & Hirth, 2006).

Although much of the mantle is assumed to be either actively deforming, or to have experienced deformation in the past, the microstructural evolution of deformed mantle under static conditions remains poorly constrained (Evans et al., 2001). This is particularly important for long-lived, presumably stable cratonic mantle regions (e.g., Pearson et al., 1995). It is thought that most Archean cratons formed as residues of large degrees of partial melting, which results in a chemically depleted residue with lower density than unmelted mantle (Jordan, 1988). The isopycnic constraint (Jordan, 1978) has allowed cratons to survive as buoyant rafts above the convecting asthenosphere. Yet cratons are not immune to disruption, as evidenced by their rifted margins, intracratonic seismic discontinuities (Hopper et al., 2014), complex anisotropy (Ford et al., 2016), and hypotheses that small cratons may be fragments of larger cratons (Bleeker, 2003). Therefore, cratonic mantle may be periodically "redeformed" during such tectonic events, thus resetting the initial mantle fabric. Because cratons have persisted for billions of years, there have been long periods of nominally static conditions between tectonic deformation events during which annealing could modify the mantle fabric.

It is challenging to decipher the history of deformation and subsequent grain growth and annealing in naturally derived mantle peridotites, because what is observed in the rocks represents an integrated tapestry of all these events. However, experiments in the laboratory on olivine aggregates have revealed important insights on deformation and annealing.

Modeling olivine grain size evolution often relies on grain growth kinetics that assume no influence of strain-energy or CPO (e.g., Shimizu, 2008) as grain growth is constrained by hydrostatic annealing of synthetic samples of pressed olivine powder (e.g., Karato, 1989). The grain growth kinetics resulting from these experiments illustrate "normal," or "continuous" grain growth, that is, where the mean of the typical log-normal distribution of grain sizes increases nonlinearly with time (Karato, 1989). However, Boneh et al. (2017) have shown that annealing of predeformed polycrystalline olivine promotes a discontinuous (i.e., abnormal) static recrystallization (DiSRX), in which recrystallization following deformation occurs by rapid growth of a small number of grains at the expense of other grains, creating a (possibly transient) bimodal grain size distribution (e.g., Drury & Urai, 1990). Similarly, while olivine CPO is usually interpreted in the context of deformation kinematics and strain magnitude (e.g., Boneh & Skemer, 2014; Nicolas et al., 1973; Tommasi et al., 1999), post-deformation DiSRX can modify an existing CPO with no additional strain, under static conditions. This change in CPO under static conditions, also referred to as "oriented grain growth," can occur when the population of grains that grow through DiSRX has a preferred orientation that differs from that of the deformation-related CPO (Boneh et al., 2017; Green, 1967; Lee et al., 2002; Rollett et al., 1989).

Annealing through discontinuous recrystallization may induce rheological softening by the rapid reduction of dislocation density (Ashby, 1970; Drury, 2005; Poirier & Guillopé, 1979; Toriumi, 1982) and mitigation of hardening effects resulting from fine grain sizes (Hansen et al., 2019; Kumamoto et al., 2017; Rutter & Brodie, 1988). Yet, it is not clear whether or in what ways DiSRX of olivine occurs under mantle conditions.

Here we combine observations from natural mantle xenoliths from the Wyoming Craton with experimental observations to (1) characterize annealed microstructures of xenoliths showing different amounts of annealing, (2) demonstrate the similarity between annealing microstructures from natural xenoliths and lab experiments, (3) discuss the conditions necessary to promote annealing through DiSRX in the mantle,

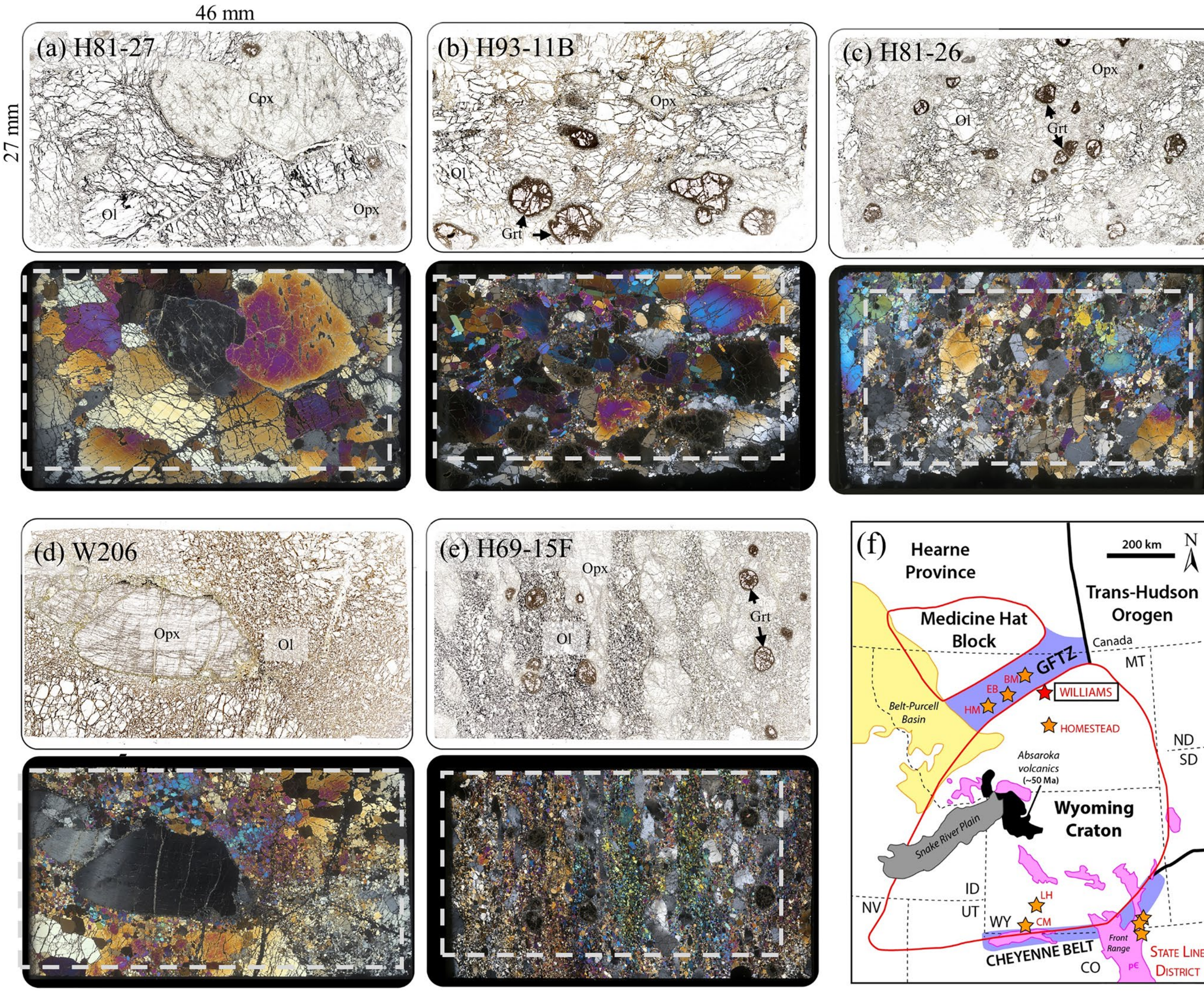

Figure 1. Peridotite xenoliths from the Williams diatreme, Wyoming Craton. (a–e) Optical micrographs with plane and cross polarized light (upper and lower, respectively) of the five samples highlighted here. Dashed line rectangle marks the bounds of the area mapped by electron backscatter diffractions shown in Figure 2. Frames for all scans are 46 mm by 27 mm. (f) Geologic and geographic map of the Wyoming craton. Williams diatreme marked by a red star and other diatremes marked by orange stars. BM, Bearpaw Mountains; CM, Cedar Mountain; EB, Eagle Butte; GFTZ, Great Falls tectonic zone; HM, Highwood Mountains; LH, Leucite Hills. Full sized crossed polarized maps can be found in the supporting Information (Figure S3).

and (4) estimate the timescales of the deformed-then-annealed kimberlitic xenoliths. Our study shows that annealing via DiSRX may be an underappreciated process for understanding the rheological evolution at the base of the lithospheric mantle.

2. Methods

2.1. Geologic Setting and Sample Description

The Wyoming Craton is a small craton of Archean age (C. T. A. Lee et al., 2011) located in the Western USA (Figure 1f). Although the Wyoming Craton has survived as a coherent block since ~2.5 Gy, its edges have been subject to tectonic and magmatic events since Proterozoic time. To the northwest, the Great Falls Tectonic Zone, last active in the Proterozoic, represents a suture stitching together the Medicine Hat Block and the Wyoming Craton (Gorman et al., 2002). To the southeast, the Cheyenne Belt is another shear zone thought to have formed during collision of island arc terranes ~1.7 Gy ago, during the final assembly of Laurentia (Karlstrom & Houston, 1984). The last major recent tectono-magmatic disruption of the Wyoming Craton occurred in the Cenozoic, where seismic tomography data (E. D. Humphreys et al., 2015) suggest that the deep, Archean mantle lithosphere of the Wyoming Craton may have been de-stabilized during the Laramide Orogeny (~75–45 Ma, Dickinson et al., 1988). Punctuated throughout this long history were episodic bursts of kimberlite and lamproite magmatism, with pulses occurring in the Devonian, Eocene, and Pliocene (Eggler et al., 1988). These kimberlites are of interest because many of them brought up deep crustal and mantle xenoliths, which provide snapshots of deep mantle processes.

We analyzed five garnet harzburgites from the Williams kimberlite diatreme (Figures 1a–1e), one of several Eocene ultramafic volcanic centers exposed along the northwestern margin of the Wyoming Craton. Peridotite xenoliths from Williams are divided into low-temperature and high-temperature groups. The low-T group consists of garnet and spinel peridotites that preserve intermineral equilibrium temperatures that fall along a typical shield geotherm (assuming heat flow of ~40 mW/m^2). The high-T group is represented by garnet peridotites recording temperatures significantly higher than a shield geotherm (Carlson et al., 1999; Hearn, 1986; Hearn & Boyd, 1975). The two groups of xenoliths also show distinct Re-depletion model ages; low-T samples reflect cooling of Archean-Paleoproterozoic mantle lithosphere, whereas high-T samples have Re-Os isotopic compositions that reflect ages not older than Neoproterozoic (Carlson et al., 1999). The chemical and isotopic differences between these two groups have led to the interpretation that the cratonic mantle keel sampled by the Williams kimberlite was recently modified by either a reheating episode or the addition of another layer of mantle lithosphere (Carlson et al., 1999, 2004; E. D. Humphreys et al., 2015).

In this study, we analyze the microstructures and crystallographic alignment in five high-T Williams xenoliths with estimated temperatures of ~1350°C and pressures ~5 GPa (summarized in Figure 10 of Hearn et al., 2004). The high-T Williams samples are characterized by distinctive textures of deformation and annealing, with a foliation defined by orthopyroxene shape preferred orientation, olivine intragrain misorientation, and a distinct symmetry of CPO (Figure 2). The samples show a small number of cracks filled by alteration minerals. These show up as white (i.e., unindexed) regions in the EBSD maps, cross-cutting large grains or across the whole sample (Figure 1a and 1d, respectively). The distinctive annealed microstructures with tablet-shaped grains observed in the high-T Williams xenoliths are not observed in the low-T Williams samples or in xenolith samples from the nearby Homestead or Bearpaw localities.

To investigate the processes governing microstructural development during annealing, we also examined microstructures produced during a deformation-then-annealing experiment conducted on Balsam-Gap dunite in a Griggs-type apparatus (Tullis & Tullis, 1986) at Brown University. The experimental sample was cored from a block of Balsam Gap dunite, which comprises ~99% olivine (with ~1% spinel) with large grains (>200 μm). For further description of the starting material, see Skemer et al. (2011) and Speciale et al. (2020). The initial water content of this material is estimated based on mass loss (approximately 0.4 wt.%) upon drying cores of the dunite starting material in a controlled atmosphere furnace at 1000°C for 10 h ($CO:CO_2 = 1:5$), suggesting trace amounts of hydrous alteration phases along grain boundaries (Speciale et al., 2020). FTIR on optically clear olivine grains in the starting material indicate an initial water content of approximately 20 ppm by weight (Speciale et al., 2020). Experiments were performed using molten salt (NaCl + KCl) as the pressure medium (e.g., Green & Borch, 1989) at a pressure of 1030 ± 20 MPa and temperatures measured by type S thermocouples (schematic illustration of the experimental assembly used is shown in Figure S1a in the Supporting Information). The sample was first deformed in axial compression to an engineering strain (i.e., change of sample length normalized by its original length) of $\varepsilon \sim 0.3$ at 1100°C and a strain-rate of 5×10^{-6}/s, resulting in a differential stress of about 300 MPa. After deformation, the sample was unloaded (to produce hydrostatic conditions) and temperature was increased to 1250°C for 2.5 h (stress-time path is available in the Supporting Information, Figure S1b). The annealing imposed after deformation simulates the annealing of a deformed mantle during a transient heating episode. We did not measure the water content of our sample after deformation; FTIR analyses of olivine grains from the samples studied by Speciale et al. (2020), deformed at 1100°C at 1 GPa, show water contents of 37 ± 19 ppm by weight.

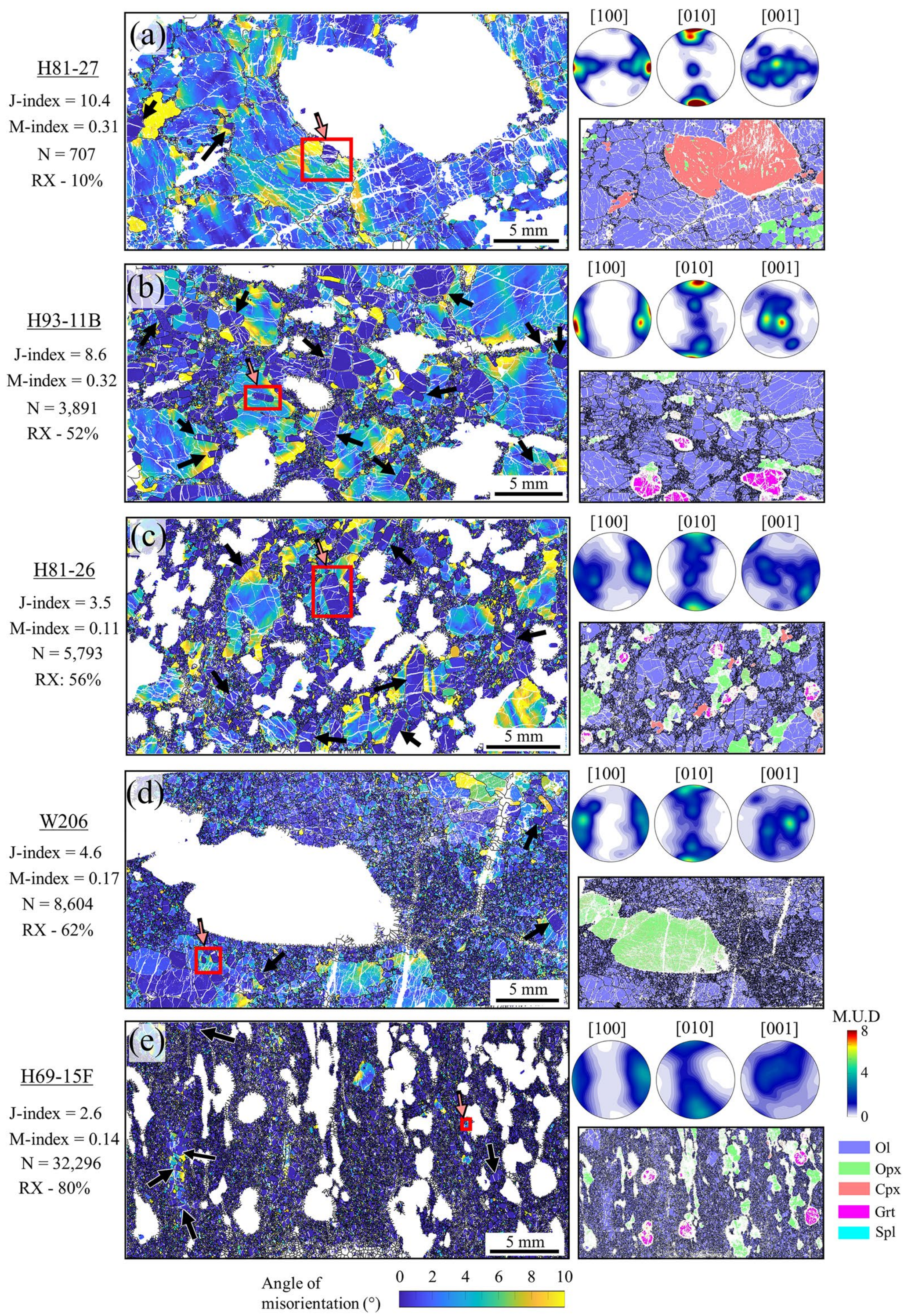

Figure 2. Peridotite xenoliths from the Williams diatreme, Wyoming Craton. Samples (a–e) are ordered by their fraction of recrystallized grains (RX). Left side: Maps of the intragrain misorientation by its internal angle of misorientation. The black arrows highlight the faceted tablet-shaped grains and the red arrows and boxes delineate areas with typical tablet-shaped grains shown in Figure 3. Upper right: Pole figures of olivine crystallographic orientations contoured by the multiple of uniform distribution (MUD). Since xenolith samples cannot be oriented to an absolute kinematic reference frame, the pole figures are plotted such that the [100], [010], and [001] olivine axes maxima were manually aligned with the *X*, *Z*, and *Y* directions, respectively (with accordance to the widely observed "A-type" olivine fabric [Ben Ismaïl & Mainprice, 1998]). Lower right: Maps illustrating the phase distribution. Phases: Cpx stands for Clinopyroxene, Grt for Garnet, Ol for Olivine, Opx for Orthopyroxene, and Spl for Spinel. Other abbreviations used: *N*, number of olivine grains. *M*-index and *J*-index = indices for texture strength (see text).

10.1029/2020GC009377

2.2. Collection and Analysis of Microstructural Data

Microstructures were analyzed using an Oxford Instruments Symmetry EBSD detector on a FEI Apreo LoVac field emission gun scanning electron microscope (SEM) at UC San Diego. Automated EBSD maps were acquired using a step size of 1–5 μm (step size varied depending on average sample grain size), at a working distance between 26 and 28 mm, and voltage of 20 kV. A higher-resolution map (step size of 0.1 μm) was acquired to resolve details in the microstructure in fine-grained regions of sample H69-15F. Raw EBSD data were filtered in CHANNEL5 by first removing wild spikes, then orientations of nonindexed pixels were iteratively filled using a nearest neighbor filling method. In most cases, filtering was minimal or not necessary as indexing rates were 90% or higher. We used the open source MTEX software (version 5.1.1) to generate and analyze the data in the EBSD maps (Bachmann et al., 2010). Pole figures were calculated as area weighted (Figure 2) using the density of the orientation distribution function with a half-width of 10° plotted on the upper hemisphere. The pole figures in Figures 2–4 contain all of the indexed pixels (area weighted) to emphasize the change of overall CPO associated with the increased fraction of recrystallization. The pole figures in Figure 6 were constructed using one point per grain to discount for the effect of grain size. Grain boundaries are defined with a minimum angle of 10°, and distortions within grain interiors are quantified using grain orientation spread, "GOS," and misorientation with respect to the grain's mean orientation, "Mis2Mean" (built-in MTEX functions). Both functions quantify the misorientations in grains due to geometrically necessary dislocations. To distinguish between deformed and recrystallized grains, a threshold of GOS = 2° is used (following Cross et al., 2017) such that grains with higher/lower GOS are classified as deformed/recrystallized grains, respectively. Of the fraction of grains with GOS<2°, the dynamically and statically recrystallized grains are categorized by their size; $d < 25$ μm and $d > 25$ μm, respectively. The strength of the CPO was quantified using the dimensionless J-index, J_{MDF} (calculated for each axis), as well as the M-index (Bunge, 1982; Mainprice et al., 2015; Skemer et al., 2005).

2.3. Temperature, Pressure, and Water Content

For those xenoliths that lack previously determined equilibration pressure and temperature constraints, we use electron microprobe data (Chilson-Parks, 2019) to apply the two-pyroxene Ca exchange geothermometer and opx-garnet Al exchange geobarometer with estimated ±20°C and ±0.3 GPa (1σ) uncertainties (Brey & Köhler, 1990). Since sample H02-9E is missing grains of cpx, we applied the opx-grt Mg-Fe exchange geothermometer with estimated uncertainty of ±40°C (Harley, 1984). These calculated final equilibration P-T's are presented with previously published P-T from Hearn (2004) and Downes et al. (2004) in Table S1.

Water contents in olivine and pyroxene grains were measured using secondary ion mass spectrometry (SIMS) on a CAMECA IMS 6F at the Department of Terrestrial Magnetism, Carnegie Institution for Science. Selected grains, hand-picked based on optical clarity, were placed in indium-filled aluminum mounts. The mounts also included one standard grain to monitor instrumental drift (basaltic glass MORB, ALV 519-4-1, 1700 μg/g H_2O) and one grain to determine detection limits (commercially available Suprasil 3002, pure SiO2 glass, 1 μg/g H_2O). Mounts were polished and then cleaned with milli-Q™ water and ethanol and stored in a 50 ºC vacuum oven for at least 12 h.

The gold-coated samples were analyzed using a primary Cs + beam at 10 kV and 20 nA with a secondary extraction voltage of −5 kV. Although sputtering pits were ∼30 μm in diameter, we limited ion transmission to the centermost 10 μm of the pit using the smallest available field aperture. Presputtering for 300 s was used to minimize surface contamination. In addition, $^{12}C/^{30}Si$ was measured to monitor contamination during analysis. Further description of the mineral standards used for calibration and the calibration curves can be found in the Supporting Information (Text S1, Figure S5, and Table S3). Although water contents were measured in both olivine and orthopyroxene, the reported olivine water contents are calculated using the average measured H_2O content in orthopyroxene and the partition coefficient of $D_{H_2O}^{Ol/Opx} = 0.11$ from Warren and Hauri (2014). This conversion from orthopyroxene to olivine H_2O concentration was applied to minimize the effect of water loss during xenolith entrainment and ascent in the host magma. Some variation in $D_{H_2O}^{Ol/Opx}$ could be introduced through the effect of Al content on the water content in orthopyroxene.

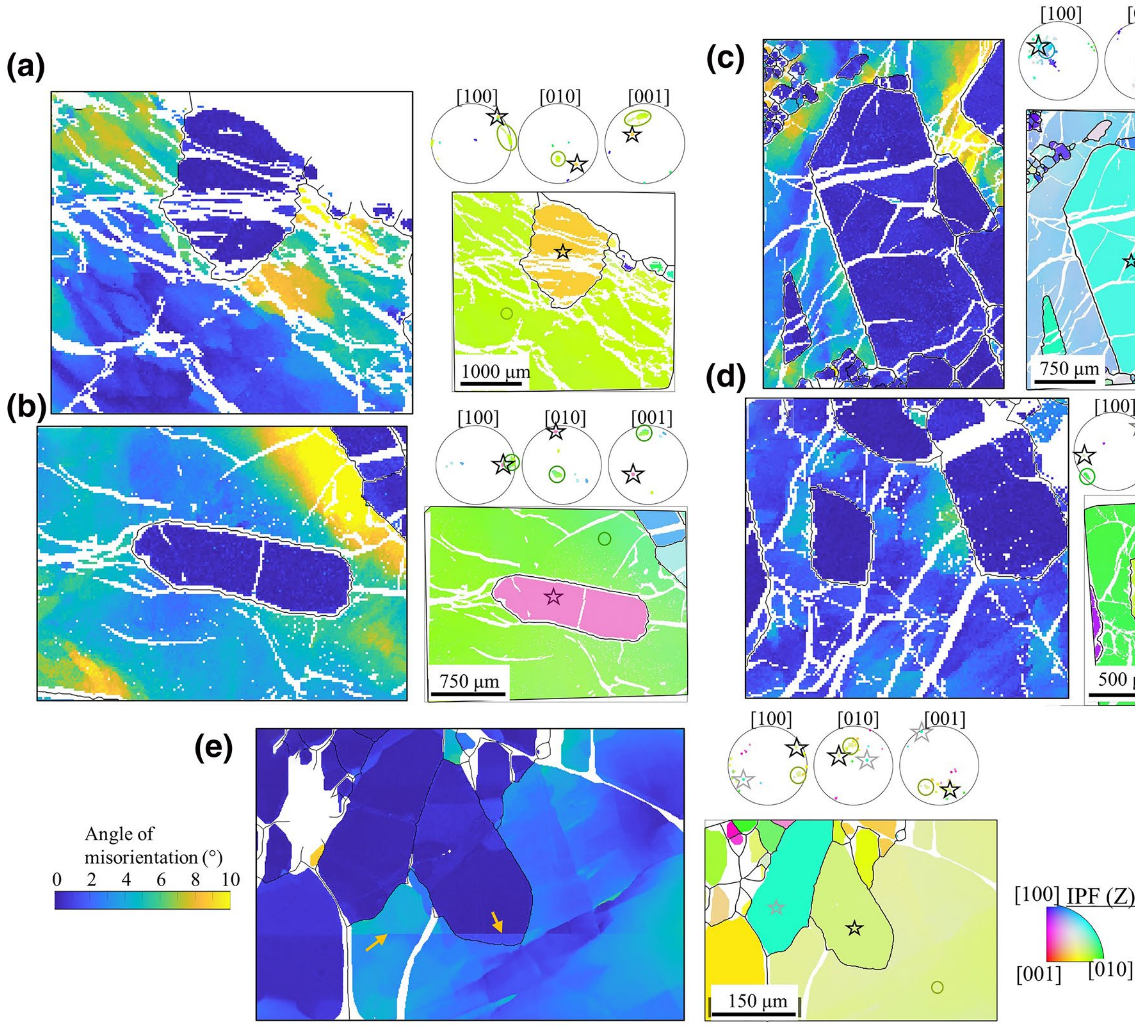

Figure 3. Evidence for discontinuous static recrystallization (DiSRX) in the xenoliths. Microstructural characterization of tablet-shaped annealed grains with faceted boundaries and low intragrain misorientation from xenolith H81-27 (a), H93-11B (b), H81-26 (c), W206 (d), and H69-15F (e). Intragrain misorientation maps (left), pole figures (upper right), and orientation maps (lower right) highlight the contrast in intragrain strain energy and the characteristic misorientation angles of 10°–20° and 90° between annealed grains and their surroundings. The locations of these maps (a–e) are delineted by the red boxes in Figures 2a–2e, respectively. (e) High-resolution map with step size of 0.1 μm. Orange arrows point to a horizontal artifact line due to a temporary charging during the run.

However, since the orthopyroxenes are generally unzoned, and exhibit low Al contents (0.03–0.05 Al^{IV}) typical of cratonic mantle, we use a constant $D_{H_2O}^{Ol/Opx}$.

3. Results

3.1. Optical Petrography

The five Williams xenoliths exhibit porphyroclastic to porphyroclastic-transitional textures (Mercier & Nicolas, 1975) (Figure 1). The matrix is dominated by variably fine-grained (~10 to ~100 μm) recrystallized olivine. Olivine porphyroclasts exhibit undulose extinction (Figure 1b and 1c). An important feature is the presence of olivine tablet-shaped grains, which are often observed to "grow" into coarser-grained olivines with large intragrain misorientations. Orthopyroxene occurs as large and bent porphyroclasts, as well as highly elongate, wavy grains with "tails" of extremely fine-grained orthopyroxene neoblasts (e.g., sample H69-15F, Figure 1e). This texture is characteristic of the fluidal-mosaic texture of Boullier and Nico-

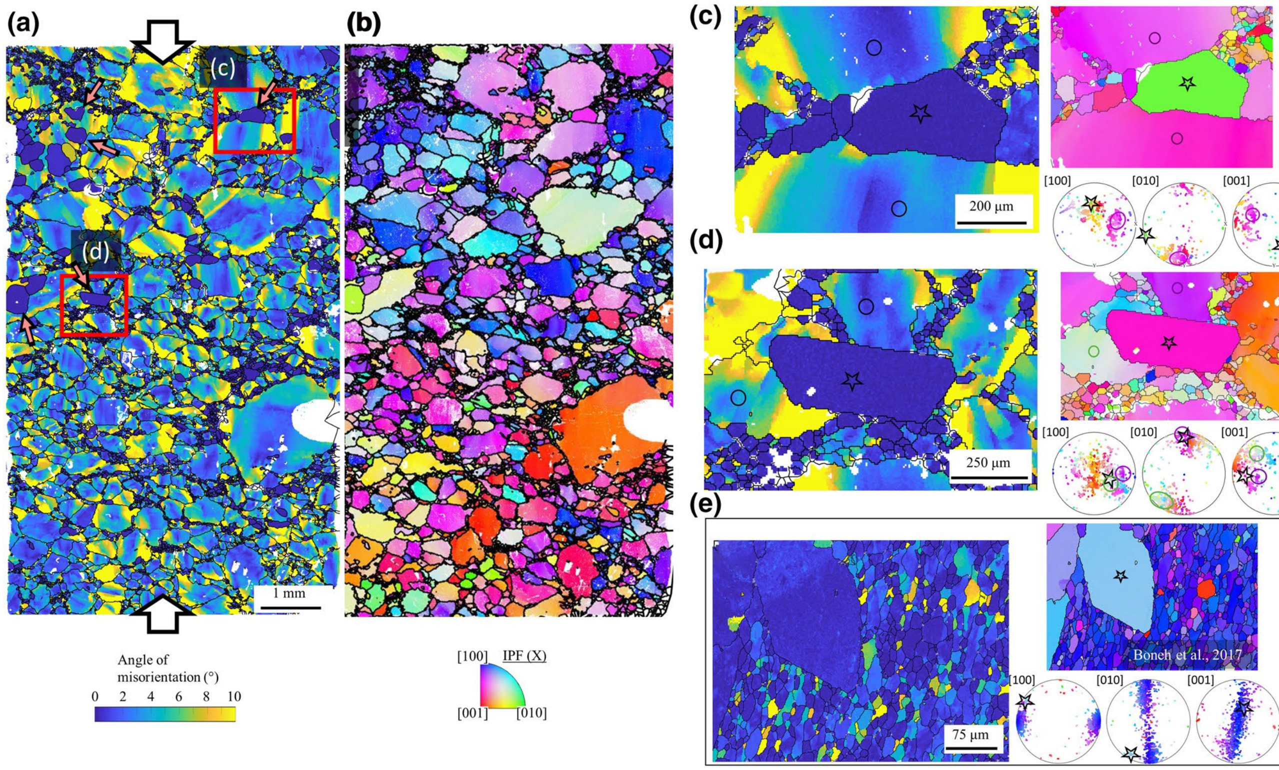

Figure 4. Experimental evidence for discontinuous static recrystallization (DiSRX). EBSD maps of intragrain misorientation orientation (left), orientation (upper right), and pole-figures (lower right; c–e) from experimental samples that experienced deformation followed by a stage of annealing. (a–d) Microstructures from sample W2306. (a and b) maps of the whole sample. (c and d) two enlargements of a tablet-shaped olivine grain delineated by two red boxes in (b) showing intragrain misorientation (upper map), orientation-colored map (lower map), and pole figures. (e) Annealing microstructure with similar characteristics from experiment F042 reported in Boneh et al. (2017).

las (1975). Clinopyroxene is not as abundant and does not appear to be as heavily deformed as orthopyroxene. Garnet is present in all xenoliths except W206, and occurs as medium to large rounded grains with cracks and kelyphite rims.

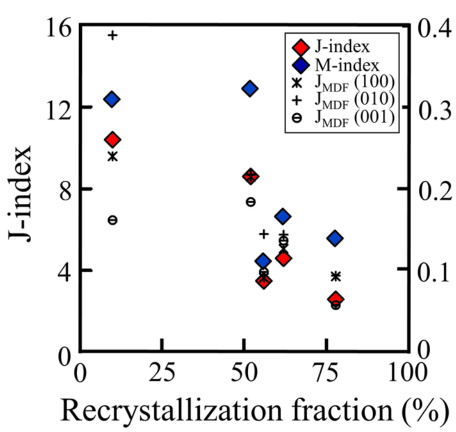

Figure 5. Crystallographic preferred orientation (CPO) strength versus fraction of recrystallization for the samples shown in Figure 2. *J*, J_{MDF}, and *M*-indices are used to quantify CPO strength (Bunge, 1982; Skemer et al., 2005).

3.2. Microstructural Characterization

Figure 2 summarizes the microstructural data (EBSD maps of phase, olivine intragranular misorientation, and pole figures of olivine CPOs) for five high-temperature garnet harzburgite samples from the Williams diatreme. Within these samples, two classes of olivine grains can be distinguished: (1) grains with high intragrain misorientations (GOS > 2°), and (2) recrystallized grains with low to negligible intragrain misorientations (GOS < 2°), which we interpret to have recrystallized either during the deformation stage (via dynamic recrystallization), or during annealing (via static recrystallization). The samples show amounts of recrystallization between 10% and 80% and similar P-T conditions (∼1350°C and 5 GPa).

The range of observed textures is highlighted in Figure 2. The sample with the smallest fraction of recrystallized grains (H81-27) exhibits large porphyroclasts (grain size ∼10 mm), small (∼10–100 μm) dynamically recrystallized grains at the boundaries, and a low number of medium-sized grains (∼1 mm) with faceted boundaries, which we interpret

10.1029/2020GC009377

to be a product of annealing (Figure 2a). By contrast, the sample showing the most evidence for annealing (H69-15F; Figure 2e), has a grain size of <250 μm and a small number of relict porphyroclasts identified by their high internal misorientation (Figure 2e).

Figure 3 shows the tablet-shaped grains characteristic of an annealed microstructure. Tablet-shaped grains have straight, faceted boundaries that crosscut grains in their immediate vicinity. The interiors of tablet-shaped grains are distinguished by very low intragrain misorientation angles as shown by the dark blue colors in the intragrain misorientation maps and are clearly distinguished from surrounding grains that show high internal misorientations (Figure 3). The contrast in the internal crystal orientations indicates that gradients in strain-energy promoted grain boundary migration during annealing. These observations suggest that deformation was followed by annealing through DiSRX. In addition, the tablet-shaped grains are misoriented relative to the CPO defined by relict grains, mostly by 10°–20° (Figure 3) and in some cases by ∼90° (e.g., Figure 3b). These characteristics can be visualized in 3D through a movie (Movie S1) showing the partially annealed microstructure of sample H93-11B; the movie was constructed using diffraction contrast tomography (LabDCT; Bachmann et al., 2019; Holzner et al., 2016).

Our microstructural analyses indicate that the Wyoming Craton xenoliths contain abundant olivine grains with characteristics of annealing of a previously deformed peridotitic mantle. Similar microstructures, including development of annealed tablet-shaped grains, were produced in the experiment in which Balsam Gap dunite was first deformed and then annealed under high temperature and static conditions (Figures 4a and 4b). Similar to the characteristics of the annealed microstructure observed in the xenoliths (Figures 2 and 3), the experimental sample shows tablet-shaped grains with a misorientation angle of 10°–20° relative to their surroundings (Figures 4c and 4d). Figure 4e shows another experimental example with similar characteristics of annealed microstructure from Boneh et al. (2017).

3.3. Texture Analysis

The xenoliths show evidence for two events based on interpretation of their microstructure. The first event is deformation and coeval grain size reduction via dynamic recrystallization. This event led to the development of large porphyroclastic grains with high internal misorientations and smaller grains with low internal misorientations located along porphyroclast boundaries. The second event corresponds to a subsequent annealing event, which produced the faceted grains that overprint deformed relict grains. We define three types of grains: (1) "porphyroclasts" or "paleoclasts" that have high internal misorientation, (2) dynamically recrystallized grains ("DRX") formed during deformation, and (3) "DiSRX" grains that formed after deformation under low stress conditions. The difference in grain orientations between relict deformed grains and annealed grains shown in Figures 3 and 4 results in an overall weaker CPO. The effect of recrystallization (with contributions from both DRX and DiSRX) on CPO can be seen by the texture strength of xenoliths with variable recrystallization fraction (defined by the threshold GOS): xenoliths with a low fraction of recrystallized grains exhibit a strong CPO, whereas xenoliths with a high fraction of recrystallized grains exhibit a weaker CPO (Figure 2). For example, H69-15F (Figure 2e) is highly recrystallized and the CPO is relatively weak with the lowest *J*-index of all five xenoliths. In H69-15F, the concentration of olivine [100] is dispersed in the *XZ* plane, [010] in the *ZY* plane, and [001] around the *Y* direction. Based on the variation of *J*-index, it is clear that CPO strength is inversely correlated with the fraction of recrystallized grains, suggesting that increasing recrystallization fraction (DRX and DiSRX) weakens the fabric (Figure 5).

However, the contribution of DRX and DiSRX to the overall recrystallized texture may differ. To distinguish between the orientations of the dynamically and statically recrystallized grains, we use the intragrain misorientation and grain size (discussed in Methods). Out of the population of grains classified as recrystallized (i.e., with low intragrain misorientation), the DRX grains are defined as grains with $d < 25$ μm, while DiSRX grains are defined as grains with $d > 25$ μm.

Figure 6 shows the orientations of the three types of grains from sample H81-26, which has a significant area fraction of the three grain types (maps showing the different subsets used in Figure 6 are shown in Figure S4). The CPO, illustrated by plotting one point-per-grain for each subset of grains illustrates the modification of the texture by DiSRX. The DRX grains and porphyroclasts show similar textures with a slightly

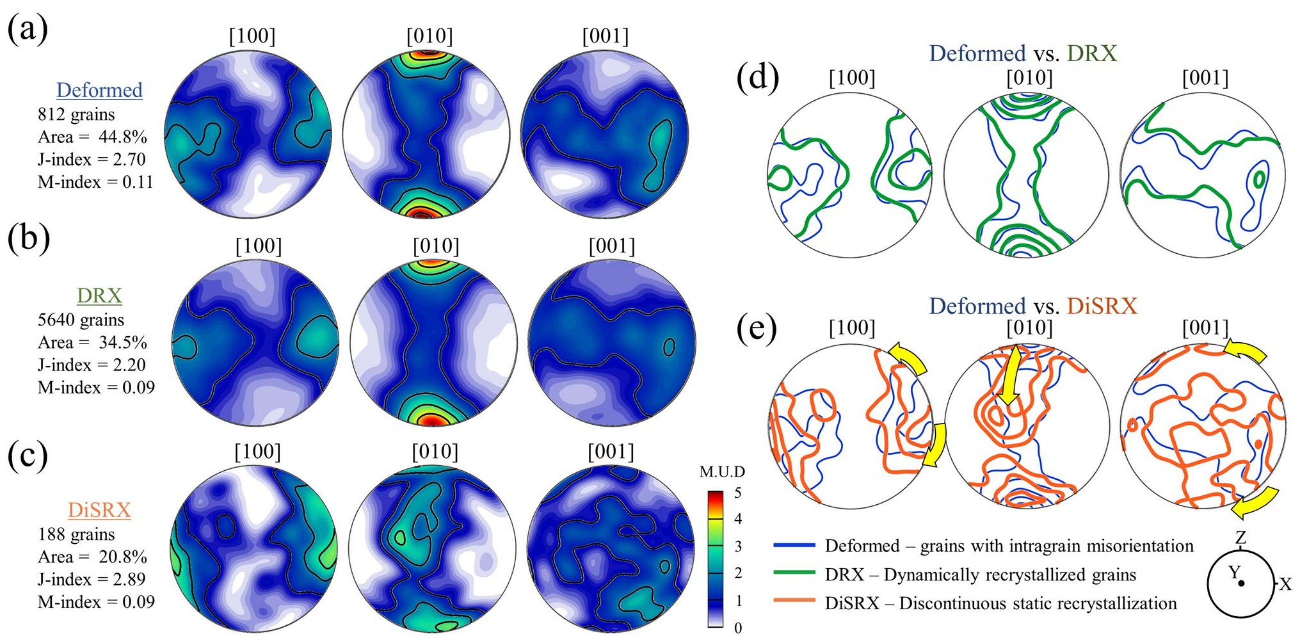

Figure 6. Pole figures from sample H81-26 contours by multiple of uniform distribution (MUD) using one point per grain for three types of olivine grain: (a) deformed, (b) dynamically recrystallized grains (DRX), and (c) discontinuously static recrystallized grains (DiSRX). (d and e) Comparison between the MUD contours of deformed (blue), DRX (green), and DiSRX (orange) highlighting the similarity between the deformed and DRX grains (d) and the orientation difference between the deformed and DiSRX grains due to annealing, illustrated by yellow arrows (e).

weaker CPO for the DRX grains (*J*-index of 2.7 and 2.2 for the deformed and DRX grains, respectively); the CPO consists of a point maximum parallel to *X* for [100], a point maximum parallel to *Z* along with a *ZY* girdle for [010], and a *XY* girdle for [001]. The pole figure for the DiSRX grains shows a modification of the CPO with a wider point maximum, stretched along the *X*-*Z* plane for [100], an additional point maximum parallel to the *Y* direction in [010], and a more random orientation spread for [001]. Although this is not a drastic change of the CPO, a fully annealed microstructure will modify the CPO both in terms of the symmetry and strength.

4. Mantle Annealing by DiSRX

Annealing, which promotes post-deformation DiSRX, is a well-studied process in material science (e.g., F. Humphreys and Hatherly, 2012) exploited to modify the strength, texture, and microstructural properties of metals and ceramics (e.g., Sakai et al., 2014; Zeng et al., 2016). Likewise, deformed mantle peridotites and crustal shear zones are expected to undergo annealing under high temperature (e.g., Borthwick et al., 2014; Boullier & Nicolas, 1975; Poirier & Guillopé, 1979; White, 1976). In this regard, some distinctions about annealing processes need to be made. Annealing reduces the energy in the system arising from crystallographic defects. Annealing could be manifested by a decrease in the intragrain strain energy through the formation of subgrain boundaries and annihilation of dislocations; annihilation is induced through the climb of free dislocations (e.g., Farla et al., 2011; Karato, 2008; Poirier, 1985). Annealing can also promote recrystallization by grain boundary migration. In this case, recrystallization is driven by gradients in strain energy density arising from deformation-induced crystal defects. Through grain boundary migration, the intragrain defects are removed leading to a modification of the grain size, grain shape, and intragrain misorientation. Under conditions where materials exhibit lower intragrain defect densities, annealing promotes normal (i.e., continuous) grain growth driven by a reduction of interfacial energy. Here we focus on annealing by DiSRX, which promotes the shift in microstructure (e.g., grain shape, size, and orientation) described above. The necessary conditions and timescales for DiSRX are discussed below.

10.1029/2020GC009377

4.1. Mantle Conditions for Annealing by DiSRX

Previous work on geologic and analog materials has shown that annealing without a component of DiSRX leads to only a minor modification of CPO (Heilbronner & Tullis, 2002; Jessell et al., 2003; Park et al., 2001). In contrast, annealing through DiSRX is likely to affect the overall CPO of a crystalline material (Boneh et al., 2017; Green, 1967; Mercier & Nicolas, 1975; Sabat & Sahoo, 2017; Stöckhert & Duyster, 1999; Urabe & Jonas, 1994). DiSRX could be a common process at the base of Earth's continental lithosphere, which, though tectonically stable over long timescales, may be heated periodically by convecting asthenosphere. For instance, the edges of cratonic areas may experience "rejuvenation" (Foley, 2008), resulting in unusual magmatism along the margins (e.g., North China Craton, Colorado Plateau). In fact, faceted olivine grains formed by annealing, similar to those reported here, have been reported before in kimberlite-hosted mantle xenoliths (Arndt et al., 2010; Mercier, 1979; Mercier & Nicolas, 1975). The prevalence of DiSRX in industrial and geomaterials can be related to the solid-state thermo-mechanical conditions (Covey-Crump, 1997; Doherty, 1997; Hidas et al., 2017). However, in many mantle xenoliths, DiSRX is typically ascribed to fluid-assisted growth during xenolith ascent in the host magma (e.g., Drury & van Roermund, 1989). It is unclear whether residence in the mantle lithosphere—including during episodic heating or tectonic events that fail to produce volcanism that bring up xenoliths—could promote DiSRX in peridotites. If DiSRX is associated with *in situ* mantle processes, this has important ramifications for interpretation of craton structure and regional seismic anisotropy.

To investigate the conditions that promote DiSRX in the mantle and to assess the role of fluids, we plot the estimated P-T's (Figure 7a) and olivine H_2O concentrations (ppm by wt., Figure 7b) from the Wyoming Craton xenoliths. We include both xenoliths with evidence for DiSRX (high-T Williams; Figure 2) and without evidence for DiSRX. The latter group includes samples from Homestead, the low-T Williams group, and Bearpaw Mountains (Figure S2), as well as experimental samples and previously characterized annealed peridotite xenoliths from the literature (See caption of Figure 7 for references). The samples that exhibit evidence for DiSRX (denoted by red outlines) all plot at higher temperatures for a given depth, indicating that the annealed microstructures tend to form at high temperature. The presence of tablet grains, which are indicative of annealing through DiSRX, does not correlate with the olivine water content of the Wyoming xenoliths (Figure 7b). For example, the high-temperature partially annealed Williams xenoliths have olivine water contents (29–33 ppm wt.) that are similar to or lower than the olivine water content of the Homestead xenoliths (26–40 ppm wt.). However, the temperatures of the Williams xenoliths (1325°C–1359°C) are higher than those of the Homestead xenoliths (1163°C–1264°C). In addition, DiSRX is observed in experimental samples that were annealed under dry or fluid undersaturated conditions (Boneh et al., 2017; Mercier, 1979; Meyers et al., 2018; Nermond, 1994). Although the water content in experiment W2306 presented here was not measured, analyses of Balsam Gap deformed under similar experimental conditions ($P = 1$ GPa and $T = 1200$°C) using the same assembly show a water content of $\sim$35 ppm wt. that originates from dehydration of a small amount of hydrous minerals in the initial sample at run conditions (Speciale et al., 2020).

Textures indicative of DiSRX have also been reported from experiments on rock analogs (Urai, 1985) and for solid-state recrystallization in kimberlitic mantle xenoliths. For the latter, the textures were interpreted to be related to kimberlite formation and represent a metasomatic event prior to eruption (Arndt et al., 2010; Cordier et al., 2015). The Wyoming xenoliths have calculated olivine water contents ($H_2O < 50$ wt. ppm) below fluid saturation ($\sim$100–200 ppm wt. at 3–5 GPa; Zhao et al., 2004), preserve PT conditions that do not cross the dry/damp solidus, and do not show consistent relationships between the calculated water content and the occurrence of DiSRX (Figure 7b). In addition, experiments under fluid undersaturated conditions produced similar microstructures indicating that a fluid-saturated environment is not a requirement for DiSRX. At undersaturated conditions, water can affect DiSRX by enhancing the kinetics of grain boundary migration and diffusion. In addition, a nanolayer of fluid at the grain boundaries has been interpreted to enhance DiSRX (Drury & van Roermund, 1989). However, fluid-induced grain boundary migration is not supported by the observations from the Wyoming Craton mantle xenoliths and lab experiments. These observations support our hypothesis that DiSRX in the mantle can be thermally induced and does not require a particularly hydrous environment.

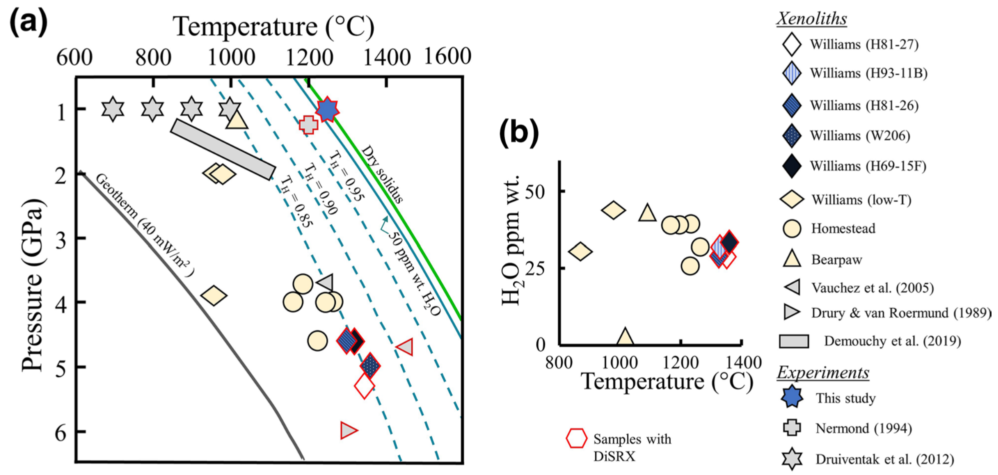

Figure 7. Pressure-temperature-H_2O relations for xenoliths from the Wyoming Craton and xenolith samples with evidence for annealing. The high-T Williams xenoliths are shown together with mantle xenoliths from nearby kimberlite diatremes of the Wyoming craton: low-T Williams, Homestead, and Bearpaw. (a) Occurrence of discontinuous static recrystallization (DiSRX) (symbols outlined in red) in temperature and pressure space. Xenoliths from South Africa (Drury & van Roermund, 1989), Tanzania (Vauchez et al., 2005), and Mongolia (Demouchy et al., 2019) are shown in gray symbols. Deformation followed by annealing experiments from this study, from Druiventak et al. (2012), and Nermond (1994) are shown. Dry and wet solidi were calculated using Hirschmann (2000) and Katz et al. (2003), respectively. Broken lines are the 0.95, 0.9, and 0.85 homologous temperature (T_H) assuming 50 ppm wt. H_2O. Geotherm of 40 mW/m^2 from Pollack and Chapman (1977). (b) Water content in ppm wt. for olivine versus temperature for the Wyoming Craton xenoliths. The water content was recalculated from measured water content in orthopyroxene using the partition coefficient form Warren and Hauri (2014); Data sources and calculated olivine water contents are reported in Table S1.

4.2. Annealing and Recovery Mechanisms in the Mantle: DiSRX Versus Grain Growth

For the DiSRX mechanism to be significant, it needs to be effective at typical mantle conditions. Apart from the effect of homologous temperature (Figure 7), the dominant driving force for grain boundary migration and grain growth will determine the microstructural response to annealing. When strain energy dominates, annealing will be governed by recrystallization processes (e.g., DiSRX), however, following recrystallization, or in cases where no deformation precedes annealing, grain growth driven by surface energy will follow. Recrystallization is, by definition, a process driven by the gradient in dislocation-density (i.e., strain energy), as opposed to normal grain growth, which is driven by the curvature of grain boundaries (i.e., surface energy). The conditions at which one mechanism (strain or surface energies) dominates are related to these driving forces for grain boundary migration (e.g., Powers & Glaeser, 1998).

Grain boundary migration occurs by diffusion across the grain boundary as the boundary migrates in the opposite direction to the flux. The mobility of a boundary (M_b) is described by the relationship:

$$M_b = \frac{V}{\Sigma F} \tag{1}$$

where V is the boundary migration velocity (m/s), and ΣF is the sum of forces acting on the boundary with units of pressure (N/m^2). The two main driving forces for boundary migration, surface energy (F_b) and strain energy (F_s), can be estimated by:

$$F_b = \frac{3\gamma}{d} \tag{2}$$

$$F_s = \mu b^2 \left(\Delta\rho\right) \tag{3}$$

where γ is the surface energy in units of (J/m^2), d is the averaged grain size of the surrounding grains (m), μ is the shear modulus (Pa), b is the length of the Burgers vector (m), and $\Delta\rho$ is the difference between dis-

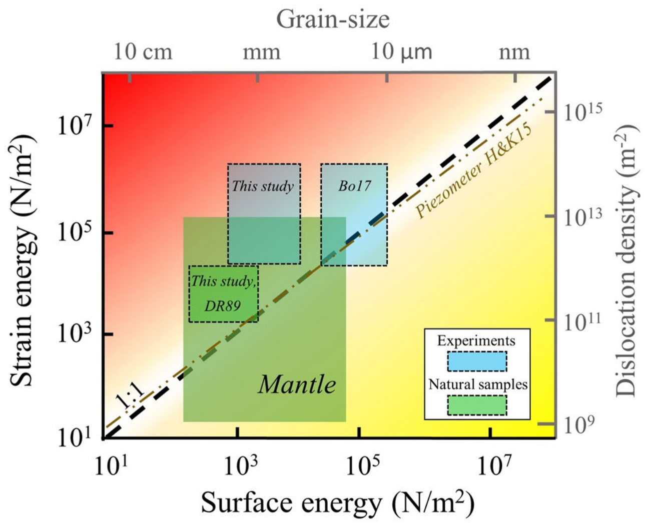

Figure 8. Parameter space of strain energy versus surface energy, the two main driving forces for recrystallization and grain size increase under static conditions. The dashed black line depicts a 1:1 ratio. The piezometer line in khaki (near the 1:1 line) uses experimentally derived piezometers for dislocation-density and grain sizes (after Hirth & Kohlstedt, 2015). Surface and strain energy were calculated using Equations 2 and 3, respectively. The green polygon represent mantle conditions calculated using a typical range of grain sizes (0.05–10 mm) and dislocation-densities (10^9–10^{13} m^{-2}). The dislocation-densities of Boneh et al. (2017) ("Bo17") and for experiment W2306 ("this study") were not measured therefore a large range of dislocation-density (10^{12}–10^{14} m^{-2}) is depicted. "DR89"—Drury and von Roermund (1989). Note that the piezometer uses dynamically recrystallized grain size while the xenolith and experimental samples are shown using the grain sizes of their porphyroclasts (representing nonsteady-state microstructure).

location-densities across the boundary (m^{-2}) (F. Humphreys & Hatherly, 2012). Using reasonable values for olivine: $\mu = 50$ GPa, $b = 0.6$ nm, and $\gamma = 0.9$ J/m^2 (Cooper & Kohlstedt, 1984), and a range of mantle grain sizes (0.05–10 mm) and olivine dislocation-densities (10^{11}–10^{13} m^{-2}) (Karato & Jung, 2003), we compare strain and surface energies for mantle conditions (Figure 8). For dislocation densities of ~10^{11}–10^{13} m^{-2} and grain sizes =>1 mm strain energy will be significantly higher than surface energy, suggesting grain size evolution controlled by DiSRX rather than normal grain growth. The ratio of these driving forces at experimental conditions (with higher stress and smaller grain sizes) scales to be similar to that inferred where DiSRX occurs in the mantle (Figure 8). In Figures 7 and 8, we delineate the temperature and strain energy conditions that lead to annealing by DiSRX in the laboratory experiments and the xenoliths.

4.3. Timescales for Grain Growth by DiSRX: Episodic Heating, Deformation, Annealing, and Kimberlite Eruption

The potential implications of DiSRX depend on the timescale at which the tablet-shaped grains form and the grain boundary mobility. Based on the microstructural similarities between xenoliths and lab samples (Figures 4 and 5), we use lab-based analyses of grain boundary mobility to assess the growth kinetics of DiSRX. Although estimates for grain boundary mobilities show significant scatter (e.g., Evans et al., 2001), a coherent trend with temperature emerges for experiments conducted at conditions where discontinuous grain growth (with or without relation to deformation) was observed, with a slope on the Arrhenius plot that is generally consistent with the individual slopes determined from the different studies (Figure 9a). The coherent trend may arise from the large driving force for grain boundary migration associated with discontinuous grain growth (e.g., high strain-energy or strongly bi-modal initial grain size), resulting in increased grain growth, which helps in measuring and quantifying the migration of a grain boundary (e.g., Piazolo et al., 2006). Using the relationship between mobility and temperature (Figure 9a), the activation energy (and pre-exponential constant) for discontinuous grain growth can be determined through the Arrhenius' equation (e.g., Huang & Humphreys, 1999):

$$M_b = M_0 e^{-Q/RT} \tag{4}$$

where M_0 is the preexponent value (m^3/s J), Q is the activation energy (J/mol), R is the gas constant, and T is the temperature (K). Linear least-squares fit between the mobility and temperature gives $Q = 133 \pm 18$ kJ/mol and $M_0 = 2 \times 10^{-11}$ m^3/s J. The activation energy is lower but comparable to that of Si grain boundary diffusion (203 ± 36 kJ/mol; Farver & Yund, 2000), but significantly lower than that for olivine creep (~300–500 kJ/mol), which may be expected for recrystallization processes (see Section 5.2.2 in Cross & Skemer, 2019).

Using Equation 4, we calculated the timescale for a small dynamically recrystallized grain to grow from 10 microns to 1 mm during annealing (Figure 9b). For this calculation, we assume a constant boundary migration-rate (V in Equation 1) and a strain energy gradient based on the range of dislocation densities appropriate for a deformed mantle (10^{11}–10^{13} m^{-2}). As shown in Figure 9b, with these assumptions we predict that the tablet grains grew by DiSRX to 1 mm in weeks to years at ~ 1300°C.

To estimate the timescale of the deformation event that occurred prior to the DiSRX, we use the P-T-H_2O conditions of the xenoliths (5 GPa, 1300°C, and 30 ppm wt., respectively) with an olivine dislocation creep flow law (Hirth & Kohlstedt, 2003) to construct a strain-rate and deformation time versus stress plot. Figure 10a shows that the range of dislocation density of ~3×10^{11}–10^{12} m^{-2} in the olivine porphyroclasts corresponds to high mantle stresses (~30–100 MPa), which promote high strain-rates (10^{-10}–10^{-8} s^{-1}). With

10.1029/2020GC009377

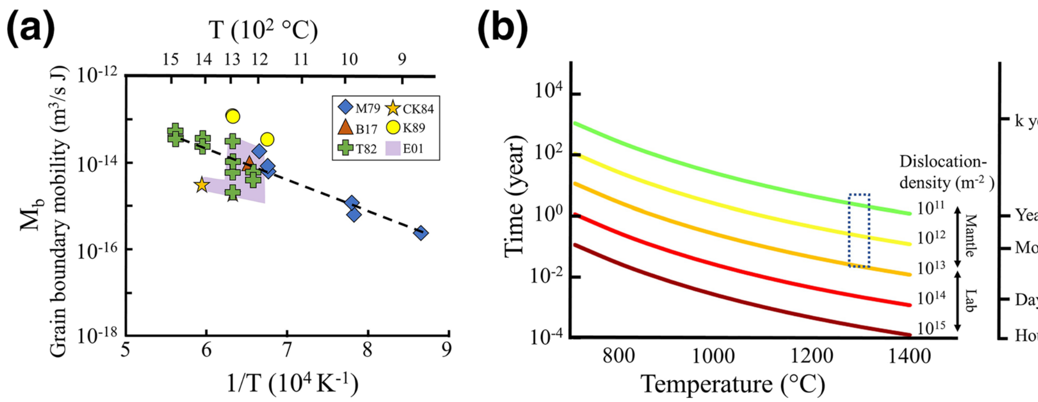

Figure 9. (a) Compilation of grain boundary mobility (M_b) against temperature from experiments with discontinuous grain growth. The purple polygon shows compilation from experiments with normal grain growth (experiments under high pressure) as a reference (Figure 2 in Evans et al., 2001). M79 (Mercier, 1979), B17 (Boneh et al., 2017), T82 (Toriumi, 1982), CK84 (Cooper & Kohlstedt, 1984), K89 (Karato, 1989), E01 (Evans et al., 2001). (b) Timescale for discontinuous grain growth of an initially 10 μm grain to 1 mm grain for different dislocation densities and temperatures. Dotted delineated area denotes the conditions for the xenolith samples of this study.

these conditions, the timescale of deformation is on the order of years to hundreds of years (Figure 10a). We speculate that the annealing occurs just after the deformation event that induced the high defect density, since the high dislocation-density samples do not show much evidence for recovery, which would have been expected at these high temperatures.

Lastly, we speculate on the timescale of heating that set the stage for the deformation and annealing events. A distinctive feature of the Williams high-T xenoliths is that, contrary to the Williams low-T, Homestead, and Bearpaw samples, the high-T xenoliths fall along a near vertical array in P-T space (Figure 7). This P-T array is not an adiabat, but is most likely caused by subsolidus mineral disequilibrium due to a transient thermal event (Chin et al., 2012). Assuming the xenoliths originally resided on a steady-state geotherm, transient heating at depth would result in rapid re-equilibration of Mg-Fe and Ca-mineral equilibria-based temperatures to the new high temperature, but the more sluggish Al-based geobarometer would not have sufficient time to re-equilibrate (cf. Chin et al., 2012), resulting in a "false adiabat." Using the order-of-magnitude relation $x = \sqrt{Dt}$, as x and t are the diffusion length and time scales, respectively and D is the diffusion coefficient with a Ca diffusivity of 10^{-14} (cm^2/s) at 1320°C (Dimanov & Jaoul, 1998), a Ca diffusion profile would be erased within ∼30,000 years in a 1 mm pyroxene grain. Since major elements are unzoned and homogeneous in pyroxene and olivine grains in the high-T xenoliths, we suggest that a transient heating event on the order of at least tens of thousands of years preceded the deformation and annealing events.

The timescales of heating, deformation, annealing, and eruption are compared in Figure 10b. The timescales for deformation and heating are both significantly greater than the timescale for annealing. The estimated timescales for all three of these processes are orders of magnitude greater than the timescale of hours expected for a kimberlitic eruption (Demouchy et al., 2006; Mercier, 1979). Similar timescales for prekimberlitic eruption processes were inferred from diffusion gradients in garnets interpreted as resulting from a fast or transient tectonic event related to the kimberlite evolution (Jollands et al., 2018). Transient heating seems to be a prerequisite for initiating the rapid deformation and annealing to form olivine tablets in the high-T Williams xenoliths, which were subsequently preserved in a successful kimberlite eruption. The origin of the heating is uncertain. One possibility is transient heating could be associated with small-scale convective anomalies at craton edges, perhaps instigated by regional tectonic deformation associated with the Laramide Orogeny, which is thought to have penetrated into the deep cratonic lithosphere (Currie & Beaumont, 2011; E. D. Humphreys et al., 2015). The Williams kimberlite, and the mantle xenoliths it bore, erupted near the edge of the Wyoming Craton and during the Laramide. However, not all of the Eocene kimberlites in the Wyoming Province contain xenoliths with olivine tablets. Since erupted kimberlites are, by nature both random and rare, we suspect that the Williams high-T xenoliths present a fortuitous record of the heating-deformation-annealing cycle that probably accompanies precursors to kimberlites, most of which never "breach" to the surface. Olivine tablets formed

10.1029/2020GC009377

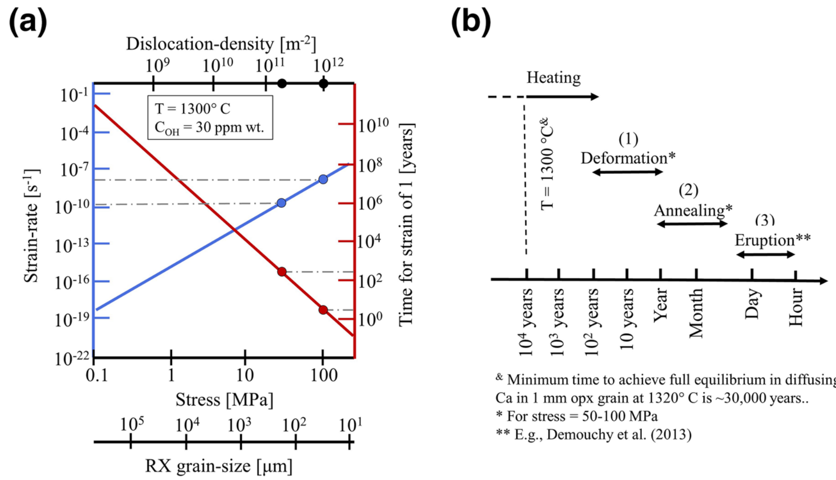

Figure 10. (a) Strain-rate (blue) and the time to achieve strain of 1 (red) against stress, dislocation-density, and the dynamically recrystallized grain-size. The stress versus strain-rate was calculated using olivine flow law for dislocation creep (Hirth & Kohlstedt, 2003), while grain sizes and dislocations-densities were calculated using appropriate piezometers from Hirth and Kohlstedt (2015) and Bai and Kohlstedt (1992), respectively. Gray lines showing the approximate dislocation-density and dynamically recrystallized grain-size in the xenolith samples. (b) A 1-D graph depicting the sequence of events and their timescale for the high-T Williams samples up to their eruption to the surface.

by DiSRX may therefore be common in the deep cratonic mantle, and the effect of DiSRX on olivine CPO and seismic anisotropy should be considered in studies of craton structure.

5. Implications and Conclusions

Deformation in the mantle is inferred through anisotropy of seismic waves and from mantle samples brought to the surface with microstructures indicative of past deformation events preserved at static low-temperature conditions or “quenched” from a current stage of deformation. The phenomenon of annealing of a deformation microstructure through DiSRX can significantly shift microstructure properties of a previously deformed mantle. Most models for mantle dynamics that include grain size evolution use the empirical relations for grain size change during deformation (dynamic recrystallization) or during static conditions (normal grain growth). It is therefore assumed, implicitly or explicitly, that after deformation ceases and hydrostatic conditions prevail, the strain energy is efficiently and quickly recovered so that further change in grain size will be due to the driving force of surface energy (e.g., Karato, 1989). However, observations both from natural xenoliths and lab-designed annealing experiments show similar characteristics manifested through strain-free grains that consume the deformed medium and consequently modify the grain size, dislocation-density, and orientation characteristics of the medium. Annealing through DiSRX will reduce the overall CPO strength and the expected seismic anisotropy. Our estimate of conditions for DiSRX reveals two main factors that invoke strain energy as the dominant driving force for DiSRX (as opposed to recovery by surface energy leading to normal grain growth): a strong temperature dependence ($T/T_m > 0.9$) and high dislocation-density in the range of 10^{11}–10^{13} m^{-2}. Fluid-assisted recrystallization may promote DiSRX under some conditions, as previously suggested (Drury & van Roermund, 1989). However, this process requires a fluid film at grain boundaries. We propose that DiSRX can also be induced through a solid-state mechanism that does not depend on the existence of fluids. We did not observe any correlation between olivine H_2O content and annealing characteristics in experiments or mantle xenoliths. Therefore, DiSRX can be effective in high-temperature regions of the mantle, where a deformed mantle goes through annealing without the necessity of fluids or wetting of grain-boundaries.

Finally, using kinetics of grain boundary migration and dislocation creep flow laws we show that the intense deformation event (stresses of 30–100 MPa based on known piezometers) and annealing through DiSRX were fast in geological time (timescales of years to hundreds of years and weeks to years, respectively) but much slower than the timescale of kimberlitic eruption (~hours). We conclude that in some cases of high temperature deformation-relaxation, deformed mantle is likely to undergo an episode of annealing that will significantly alter its microstructural, rheological and seismological properties. The full range of implications of annealing for mantle rheology (such as softening related to the microstructural recovery or grain size sensitive processes) or seismic properties (anisotropy, attenuation) opens up further avenues for future studies on mantle annealing and kimberlite related processes.

Data Availability Statement

In addition to the data used in this article through figures, tables, and supporting information, the experiment mechanical data are available through a public domain repository OSF (https://osf.io/n8t9a/).

Acknowledgment
This work was supported by NSF EAR 1719208 to EJC and NSF-EAR 1361487 to AES and GH. The authors wish to thank Reid Cooper for constructive discussions, Ningli Zhao for assistance in performing the deformation-annealing experiment and Jianhua Wang for assistance operating the SIMS. In addition, we would like to thank Dr. Jette Oddershede (Xnovo Technology) for constructing the 3D absorption contrast tomography images (LabDCT) for sample H93-11B (Movie S1). Review of Vasileios Chatzaras and two anonymous reviewers greatly contributed to the quality of the paper.

References

Arndt, N., Guitreau, M., Boullier, A.-M., Le Roex, A., Tommasi, A., Cordier, P., & Sobolev, A. (2010). Olivine, and the origin of kimberlite. *Journal of Petrology*, *51*, 573–602.

Ashby, M. F. (1970). The deformation of plastically non-homogeneous materials. *The Philosophical Magazine: A Journal of Theoretical Experimental and Applied Physics*, *21*(170), 399–424.

Bachmann, F., Bale, H., Gueninchault, N., Holzner, C., & Lauridsen, E. M. (2019). 3D grain reconstruction from laboratory diffraction contrast tomography. *Journal of Applied Crystallography*, *52*(3). 643–651.

Bachmann, F., Hielscher, R., & Schaeben, H. (2010). Texture analysis with MTEX–free and open source software toolbox. *Solid State Phenomena*, *160*, 63–68.

Bai, Q., & Kohlstedt, D. L. (1992). High-temperature creep of olivine single crystals, 2. Dislocation structures. *Tectonophysics*, *206*(1–2), 1–29.

Ben Ismaïl, W., & Mainprice, D. (1998). An olivine fabric database: an overview of upper mantle fabrics and seismic anisotropy. *Tectonophysics*, *296*(1–2), 145–157.

Bleeker, W. (2003). The late Archean record: A puzzle in ca. 35 pieces. *Lithos*, *71*(2–4), 99–134.

Boneh, Y., & Skemer, P. (2014). The effect of deformation history on the evolution of olivine CPO. *Earth and Planetary Science Letters*, *406*, 213–222.

Boneh, Y., Wallis, D., Hansen, L. N., Krawczynski, M. J., & Skemer, P. (2017). Oriented grain growth and modification of 'frozen anisotropy'in the lithospheric mantle. *Earth and Planetary Science Letters*, *474*, 368–374.

Borthwick, V. E., Piazolo, S., Evans, L., Griera, A., & Bons, P. D. (2014). What happens to deformed rocks after deformation? A refined model for recovery based on numerical simulations. *Geological Society, London, Special Publications*, *394*, 215–234.

Boullier, A. M., & Nicolas, A. (1975). Classification of textures and fabrics of peridotite xenoliths from South African kimberlites. *Physics and Chemistry of the Earth*, *9*, 467–468.

Brey, G., & Köhler, T. (1990). Geothermobarometry in four-phase lherzolites II. New thermobarometers, and practical assessment of existing thermobarometers. *Journal of Petrology*, *31*, 1353–1378.

Bunge, H.-J. (1982). *Texture analysis in materials science* (p. 593). London, UK: Butterworths. http://dx.doi.org/10.1016/B978-0-408-10642-9.50019-2

Carlson, R. W., Irving, A., & Hearn, B. (1999). *Chemical and isotopic systematics of peridotite xenoliths from the Williams kimberlite, Montana: Clues to processes of lithosphere formation, modification and destruction*. Proceedings of the VIIth International Kimberlite Conference, University of Cape Town Rondebosch, South Africa (pp. 90–98).

Carlson, R. W., Irving, A. J., Schulze, D. J., & Hearn, B. C., Jr. (2004). Timing of Precambrian melt depletion and Phanerozoic refertilization events in the lithospheric mantle of the Wyoming Craton and adjacent Central Plains Orogen. *Lithos*, *77*(1–4), 453–472.

Chilson-Parks, B. H. (2019). *The geochemistry of Cenozoic volcanism in the Andean southern volcanic zone, 34ºS-38ºS: Evaluating the role of Subcontinental lithospheric mantle in Alkali magma petrogenesis* (Doctoral dissertation). Providence, RI: Brown University.

Chin, E. J., Lee, C. T. A., Luffi, P., & Tice, M. (2012). Deep lithospheric thickening and refertilization beneath continental arcs: Case study of the P, T and compositional evolution of peridotite xenoliths from the Sierra Nevada, California. *Journal of Petrology*, *53*(3), 477–511.

Christensen, N. I. (1984). The magnitude, symmetry and origin of upper mantle anisotropy based on fabric analyses of ultramafic tectonites. *Geophysical Journal International*, *76*, 89–111.

Cooper, R., & Kohlstedt, D. (1984). Sintering of olivine and olivine-basalt aggregates. *Physics and Chemistry of Minerals*, *11*, 5–16.

Cordier, C., Sauzeat, L., Arndt, N. T., Boullier, A.-M., Batanova, V., & Barou, F. (2015). Metasomatism of the lithospheric mantle immediately precedes kimberlite eruption: new evidence from olivine composition and microstructures. *Journal of Petrology*, *56*, 1775–1796.

Covey-Crump, S. (1997). The high temperature static recovery and recrystallization behaviour of cold-worked Carrara marble. *Journal of Structural Geology*, *19*, 225–241.

Cross, A. J., Prior, D. J., Stipp, M., & Kidder, S. (2017). The recrystallized grain size piezometer for quartz: An EBSD-based calibration. *Geophysical Research Letters*, *44*(13), 6667–6674. https://doi.org/10.1002/2017GL07383

Cross, A. J., & Skemer, P. (2019). Rates of dynamic recrystallization in geologic materials. *Journal of Geophysical Research: Solid Earth*, *124*, 1324–1342. https://doi.org/10.1029/2018JB016201

Currie, C. A., & Beaumont, C. (2011). Are diamond-bearing Cretaceous kimberlites related to low-angle subduction beneath western North America? *Earth and Planetary Science Letters*, *303*(1–2), 59–70.

Demouchy, S., Tommasi, A., Ionov, D., Higgie, K., & Carlson, R. W. (2019). Microstructures, water contents, and seismic properties of the mantle lithosphere beneath the northern limit of the Hangay Dome, Mongolia. *Geochemistry, Geophysics, Geosystems*, *20*(1), 183–207. https://doi.org/10.1029/2018GC007931

Demouchy, S., Jacobsen, S. D., Gaillard, F., & Stern, C. R. (2006). Rapid magma ascent recorded by water diffusion profiles in mantle olivine. *Geology*, *34*(6), 429–432.

Dickinson, W. R., Klute, M. A., Hayes, M. J., Janecke, S. U., Lundin, E. R., McKittrick, M. A., & Olivares, M. D. (1988). Paleogeographic and paleotectonic setting of Laramide sedimentary basins in the central Rocky Mountain region. *Geological Society of America Bulletin*, *100*(7), 1023–1039.

10.1029/2020GC009377

Dimanov, A., & Jaoul, O. (1998). Calcium self-diffusion in diopside at high temperature: implications for transport properties. *Physics and Chemistry of Minerals*, *26*(2), 116–127.

Doherty, R. D. (1997). Recrystallization and texture. *Progress in Materials Science*, *42*(1–4), 39–58.

Downes, H., Macdonald, R., Upton, B. G., Cox, K. G., Bodinier, J.-l., Mason, P. R., et al. (2004). Ultramafic xenoliths from the Bearpaw Mountains, Montana, USA: Evidence for multiple metasomatic events in the lithospheric mantle beneath the Wyoming craton. *Journal of Petrology*, *45*, 1631–1662.

Druiventak, A., Matysiak, A., Renner, J., & Trepmann, C. A. (2012). Kick-and-cook experiments on peridotite: simulating coseismic deformation and post-seismic creep. *Terra Nova*, *24*, 62–69.

Drury, M. R. (2005). Dynamic recrystallization and strain softening of olivine aggregates in the laboratory and the lithosphere. *Geological Society, London, Special Publications*, *243*, 143–158.

Drury, M. R., & Urai, J. L. (1990). Deformation-related recrystallization processes. *Tectonophysics*, *172*(3–4), 235–253.

Drury, M. R., & van Roermund, H. L. M. (1989). Fluid assisted recrystallization in upper mantle peridotite xenoliths from kimberlites. *Journal of Petrology*, *30*, 133–152.

Eggler, D. H., Meen, J. K., Welt, F., Dudas, F. O., Furlong, K. P., McCallum, M. E., & Carlson, R. W. (1988). Tectonomagmatism of the Wyoming province. *Colorado School of Mines Quarterly*, *83*(2), 25–40.

Evans, B., Renner, J., & Hirth, G. (2001). A few remarks on the kinetics of static grain growth in rocks. *International Journal of Earth Sciences*, *90*, 88–103.

Farla, R. J. M., Kokkonen, H., Gerald, J. F., Barnhoorn, A., Faul, U. H., & Jackson, I. (2011). Dislocation recovery in fine-grained polycrystalline olivine. *Physics and Chemistry of Minerals*, *38*(5), 363–377.

Farver, J. R., & Yund, R. A. (2000). Silicon diffusion in forsterite aggregates: Implications for diffusion accommodated creep. *Geophysical Research Letters*, *27*, 2337–2340.

Foley, S. F. (2008). Rejuvenation and erosion of the cratonic lithosphere. *Nature Geoscience*, *1*(8), 503–510.

Ford, H. A., Long, M. D., & Wirth, E. A. (2016). Midlithospheric discontinuities and complex anisotropic layering in the mantle lithosphere beneath the Wyoming and Superior Provinces. *Journal of Geophysical Research: Solid Earth*, *121*(9), 6675–6697. https://doi.org/10.1002/2016JB012978

Gorman, A. R., Clowes, R. M., Ellis, R. M., Henstock, T. J., Levander, A., Spence, G. D., et al. (2002). Deep probe: Imaging the roots of western North America. *Canadian Journal of Earth Sciences*, *39*(3), 375–398.

Green, H. W. (1967). Quartz: Extreme preferred orientation produced by annealing. *Science*, *157*, 1444–1447.

Green, H. W., & Borch, R. S. (1989). A new molten salt cell for precision stress measurement at high pressure. *European Journal of Mineralogy*, 213–220.

Gueguen, Y., & Darot, M. (1980). Microstructures and Stresses in Naturally Deformed Peridotites. In Scheidegger A. E. (Ed.), *Tectonic Stresses in the Alpine-Mediterranean Region. Rock Mechanics / Felsmechanik / Mécanique des Roches* (Vol *9*). Vienna, Austria: Springer. https://doi.org/10.1007/978-3-7091-8588-9_17

Hansen, L. N., Kumamoto, K. M., Thom, C. A., Wallis, D., Durham, W. B., Goldsby, D. L., et al. (2019). Low-temperature plasticity in olivine: Grain size, strain hardening, and the strength of the lithosphere. *Journal of Geophysical Research: Solid Earth*, *124*(6), 5427–5449.

Harley, S. L. (1984). An experimental study of the partitioning of Fe and Mg between garnet and orthopyroxene. *Contributions to Mineralogy and Petrology*, *86*(4), 359–373.

Hearn, J. B. C. (1986). *Alkalic ultramafic magmas in north-central Montana, USA: Genetic connections of alnoite, kimberlite and carbonatite* (4, pp. 33–35). Paper presented at International Kimberlite Conference: Extended Abstracts.

Hearn, J. B. C. (2004). The Homestead kimberlite, central Montana, USA: Mineralogy, xenocrysts, and upper-mantle xenoliths. *Lithos*, *77*, 473–491.

Hearn Jr, B.C. & Boyd, F.R. (1975). Garnet peridotite xenoliths in a Montana, USA, kimberlite. In *Physics and Chemistry of the Earth* (pp. 247-255). Pergamon.

Heilbronner, R., & Tullis, J. (2002). The effect of static annealing on microstructures and crystallographic preferred orientations of quartzites experimentally deformed in axial compression and shear. *Geological Society, London, Special Publications*, *200*, 191–218.

Hidas, K., Tommasi, A., Mainprice, D., Chauve, T., Barou, F., & Montagnat, M. (2017). Microstructural evolution during thermal annealing of ice-Ih. *Journal of Structural Geology*, *99*, 31–44.

Hirschmann, M. M. (2000). Mantle solidus: Experimental constraints and the effects of peridotite composition. *Geochemistry, Geophysics, Geosystems*, *1*(10). https://doi.org/10.1029/2000GC000070

Hirth, G., & Kohlstedt, D. (2003). Rheology of the upper mantle and the mantle wedge: A view from the experimentalists. *Inside the Subduction Factory*, *138*, 83–105.

Hirth, G., & Kohlstedt, D. L. (2015). The stress dependence of olivine creep rate: Implications for extrapolation of lab data and interpretation of recrystallized grain size. *Earth and Planetary Science Letters*, *418*, 20–26.

Holzner, C., Lavery, L., Bale, H., Merkle, A., McDonald, S., Withers, P., et al. (2016). Diffraction contrast tomography in the laboratory–applications and future directions. *Microscopy Today*, *24*(4), 34–43.

Hopper, E., Ford, H. A., Fischer, K. M., Lekic, V., & Fouch, M. J. (2014). The lithosphere–asthenosphere boundary and the tectonic and magmatic history of the northwestern United States. *Earth and Planetary Science Letters*, *402*, 69–81.

Huang, Y., & Humphreys, F. (1999). Measurements of grain boundary mobility during recrystallization of a single-phase aluminium alloy. *Acta Materialia*, *47*, 2259–2268.

Humphreys, F., & Hatherly, M. (2012). *Recrystallization and related annealing phenomena*: Elsevier. https://doi.org/10.1016/B978-0-08-044164-1.X5000-2

Humphreys, E. D., Schmandt, B., Bezada, M. J., & Perry-Houts, J. (2015). Recent craton growth by slab stacking beneath Wyoming. *Earth and Planetary Science Letters*, *429*, 170–180.

Jessell, M., Kostenko, O., & Jamtveit, B. (2003). The preservation potential of microstructures during static grain growth. *Journal of Metamorphic Geology*, *21*, 481–491.

Jollands, M. C., Hanger, B. J., Yaxley, G. M., Hermann, J., & Kilburn, M. R. (2018). Timescales between mantle metasomatism and kimberlite ascent indicated by diffusion profiles in garnet crystals from peridotite xenoliths. *Earth and Planetary Science Letters*, *481*, 143–153.

Jordan, T. H. (1978). Composition and development of the continental tectosphere. *Nature*, *274*(5671), 544–548. https://doi.org/10.1038/274544a0

Jordan, T. H. (1988). Structure and formation of the continental tectosphere. *Journal of Petrology*, *Special Volume*, (1), 11–37. https://doi.org/10.1093/petrology/Special_Volume.1.11

Karato, S. I. (1989). Grain growth kinetics in olivine aggregates. *Tectonophysics*, *168*, 255–273.

Karato, S. I. (2008). *Deformation of earth materials: An introduction to the rheology of solid earth* (p. 463). Cambridge University Press. https://doi.org/10.1017/CBO9780511804892

Karato, S. I., & Jung, H. (2003). Effects of pressure on high-temperature dislocation creep in olivine. *Philosophical Magazine*, *83*(3), 401–414.

Karlstrom, K. E., & Houston, R. S. (1984). The Cheyenne belt: Analysis of a Proterozoic suture in southern Wyoming. *Precambrian Research*, *25*(4), 415–446.

Katz, R. F., Spiegelman, M., & Langmuir, C. H. (2003). A new parameterization of hydrous mantle melting. *Geochemistry, Geophysics, Geosystems*, *4*(9). https://doi.org/10.1029/2002GC000433

Kumamoto, K. M., Thom, C. A., Wallis, D., Hansen, L. N., Armstrong, D. E., Warren, J. M., et al. (2017). Size effects resolve discrepancies in 40 years of work on low-temperature plasticity in olivine. *Science advances*, *3*, e1701338.

Lee, K. H., Jiang, Z., & Karato, S. I. (2002). A scanning electron microscope study of the effects of dynamic recrystallization on lattice preferred orientation in olivine. *Tectonophysics*, *351*(4), 331–341.

Lee, C. T. A., Luffi, P., & Chin, E. J. (2011). Building and destroying continental mantle. *Annual Review of Earth and Planetary Sciences*, *39*, 59–90.

Long, M. D., & Becker, T. W. (2010). Mantle dynamics and seismic anisotropy. *Earth and Planetary Science Letters*, *297*, 341–354.

Mainprice, D., Bachmann, F., Hielscher, R., & Schaeben, H. (2015). Descriptive tools for the analysis of texture projects with large datasets using MTEX: Strength, symmetry and components. *Geological Society, London, Special Publications*, *409*(1), 251–271.

Mercier, J. C. C. (1979). Peridotite xenoliths and the dynamics of kimberlite intrusion. In F. Boyd & H. O. Meyer (Eds.), *The mantle sample: Inclusion in kimberlites and other volcanic* (Vol. 16, pp. 197–212). https://doi.org/10.1029/SP016p0197

Mercier, J. C. C., & Nicolas, A. (1975). Textures and fabrics of upper-mantle peridotites as illustrated by xenoliths from basalts. *Journal of Petrology*, *16*(1), 454–487.

Meyers, C. D., Kohlstedt, D. L., Zimmerman, M. E., & Kruckenberg, S. C. (2018). *Microstructural recovery of experimentally deformed olivine rocks*. Paper presented at AGU Fall Meeting Abstracts. (MR31B-0083).

Nermond, S. (1994). Etude expérimentale de la recristallisation statique et de la cinétique de croissance de l'olivine (Doctoral dissertation), 7, Paris, France.

Nicolas, A., Boudier, F., & Boullier, A. M. (1973). Mechanism of flow in naturally and experimentally deformed peridotites. *American Journal of Science*, *273*, 853–876.

Park, Y., Ree, J.-H., & Kim, S. (2001). Lattice preferred orientation in deformed-then-annealed material: Observations from experimental and natural polycrystalline aggregates. *International Journal of Earth Sciences*, *90*, 127–135.

Pearson, D. G., Carlson, R. W., Shirey, S. B., Boyd, F. R., & Nixon, P. H. (1995). Stabilisation of Archaean lithospheric mantle: A ReOs isotope study of peridotite xenoliths from the Kaapvaal craton. *Earth and Planetary Science Letters*, *134*(3–4), 341–357.

Piazolo, S., Bestmann, M., Prior, D., & Spiers, C. (2006). Temperature dependent grain boundary migration in deformed-then-annealed material: Observations from experimentally deformed synthetic rocksalt. *Tectonophysics*, *427*, 55–71.

Poirier, J. P. (1985). *Creep of crystals: High-temperature deformation processes in metals, ceramics and minerals*: Cambridge University Press.

Poirier, J. P., & Guillopé, M. (1979). Deformation induced recrystallization of minerals. *Bulletin de Mineralogie*, *102*(2), 67–74.

Pollack, H. N., & Chapman, D. S. (1977). On the regional variation of heat flow, geotherms, and lithospheric thickness. *Tectonophysics*, *38*(3–4), 279–296.

Powers, J., & Glaeser, A. (1998). Grain boundary migration in ceramics. *Interface Science*, *6*, 23–39.

Rollett, A. D., Srolovitz, D. J., & Anderson, M. P. (1989). Simulation and theory of abnormal grain growth-anisotropic grain boundary energies and mobilities. *Acta Metallurgica*, *37*(4), 1227–1240.

Rutter, E. H., & Brodie, K. H. (1988). The role of tectonic grain size reduction in the rheological stratification of the lithosphere. *Geologische Rundschau*, *77*(1), 295–307.

Sabat, R. K., & Sahoo, S. K. (2017). An 'ex situ'electron backscattered diffraction study of nucleation and grain growth in pure magnesium. *Materials & Design*, *116*, 65–76.

Sakai, T., Belyakov, A., Kaibyshev, R., Miura, H., & Jonas, J. J. (2014). Dynamic and post-dynamic recrystallization under hot, cold and severe plastic deformation conditions. *Progress in Materials Science*, *60*, 130–207.

Shimizu, I. (2008). Theories and applicability of grain size piezometers: The role of dynamic recrystallization mechanisms. *Journal of Structural Geology*, *30*(7), 899–917.

Skemer, P., & Hansen, L. N. (2016). Inferring upper-mantle flow from seismic anisotropy: An experimental perspective. *Tectonophysics*, *668*, 1–14.

Skemer, P., Katayama, I., Jiang, Z., & Karato, S. I. (2005). The misorientation index: Development of a new method for calculating the strength of lattice-preferred orientation. *Tectonophysics*, *411*(1–4), 157–167.

Skemer, P., Sundberg, M., Hirth, G., & Cooper, R. (2011). Torsion experiments on coarse-grained dunite: Implications for microstructural evolution when diffusion creep is suppressed. *Geological Society, London, Special Publications*, *360*(1), 211–223.

Speciale, P. A., Behr, W. M., Hirth, G., & Tokle, L. (2020). Rates of olivine grain growth during dynamic recrystallization and post-deformation annealing. *Journal of Geophysical Research: Solid Earth*, *125*(11), https://doi.org/10.1029/2020JB020415

Stöckhert, B., & Duyster, J. (1999). Discontinuous grain growth in recrystallised vein quartz—Implications for grain boundary structure, grain boundary mobility, crystallographic preferred orientation, and stress history. *Journal of Structural Geology*, *21*(10), 1477–1490.

Tommasi, A., Tikoff, B., & Vauchez, A. (1999). Upper mantle tectonics: three-dimensional deformation, olivine crystallographic fabrics and seismic properties. *Earth and Planetary Science Letters*, *168*(1–2), 173–186.

Toriumi, M. (1982). Grain boundary migration in olivine at atmospheric pressure. *Physics of the Earth and Planetary Interiors*, *30*, 26–35.

Tullis, T. E., & Tullis, J. (1986). Experimental rock deformation techniques. In Mineral and rock deformation: Laboratory studies (36, pp. 297–324). Washington, DC: American Geophysical Union.

Twiss, R. J. (1977). Theory and applicability of a recrystallized grain size paleopiezometer. In Wyss M. (Ed.), *Stress in the Earth. Contributions to Current Research in Geophysics (CCRG)*. Basel, Switzerland: Birkhäuser. https://doi.org/10.1007/978-3-0348-5745-1_13

Urabe, T., & Jonas, J. J. (1994). Modeling texture change during the recrystallization of an IF steel. *ISIJ International*, *34*(5), 435–442.

Urai, J. L. (1985). Water-enhanced dynamic recrystallization and solution transfer in experimentally deformed carnallite. *Tectonophysics*, *120*, 285–317.

Urai, J. L., Means, W.D. & Lister, G.S (1986). Dynamic recrystallization of minerals. In B. Hobbs & H. Heard (Eds.), *Mineral and Rock Deformation*. https://doi.org/10.1029/GM036p0161

Van der Wal, D., Chopra, P., Drury, M., & Gerald, J. F. (1993). Relationships between dynamically recrystallized grain size and deformation conditions in experimentally deformed olivine rocks. *Geophysical Research Letters*, *20*, 1479–1482.

Vauchez, A., Dineur, F., & Rudnick, R. (2005). Microstructure, texture and seismic anisotropy of the lithospheric mantle above a mantle plume: Insights from the Labait volcano xenoliths (Tanzania). *Earth and Planetary Science Letters*, *232*, 295–314.
Warren, J. M., & Hauri, E. H. (2014). Pyroxenes as tracers of mantle water variations. *Journal of Geophysical Research: Solid Earth*, *119*, 1851–1881. https://doi.org/10.1002/2013JB010328
Warren, J. M., & Hirth, G. (2006). Grain size sensitive deformation mechanisms in naturally deformed peridotites. *Earth and Planetary Science Letters*, *248*(1–2), 438–450. https://doi.org/10.1016/j.epsl.2006.06.006
White, S. (1976). A discussion on natural strain and geological structure—The effects of strain on the microstructures, fabrics, and deformation mechanisms in quartzites. *Philosophical Transactions of the Royal Society of London. Series A, Mathematical and Physical Sciences*, *283*(1312), 69–86.
Zeng, Z. R., Zhu, Y. M., Xu, S. W., Bian, M. Z., Davies, C. H. J., Birbilis, N., & Nie, J. F. (2016). Texture evolution during static recrystallization of cold-rolled magnesium alloys. *Acta Materialia*, *105*, 479–494.
Zhao, Y. H., Ginsberg, S. B., & Kohlstedt, D. L. (2004). Solubility of hydrogen in olivine: Dependence on temperature and iron content. *Contributions to Mineralogy and Petrology*, *147*(2), 155–161.

References From the Supporting Information

Aubaud, C., Withers, A. C., Hirschmann, M. M., Guan, Y., Leshin, L. A., Mackwell, S. J., & Bell, D. R. (2007). Intercalibration of FTIR and SIMS for hydrogen measurements in glasses and nominally anhydrous minerals. *American Mineralogist*, *92*, 811–828.
Hauri, E., Wang, J., Dixon, J. E., King, P. L., Mandeville, C., & Newman, S. (2002). SIMS analysis of volatiles in silicate glasses: 1. Calibration, matrix effects and comparisons with FTIR. *Chemical Geology*, *183*(1–4), 99–114.
Koga, K., Hauri, E., Hirschmann, M., & Bell, D. (2003). Hydrogen concentration analyses using SIMS and FTIR: comparison and calibration for nominally anhydrous minerals. *Geochemistry, Geophysics, Geosystems*, *4*(2), https://doi.org/10.1029/2002GC000378
Kumamoto, K. M., Warren, J. M., & Hauri, E. H. (2017). New SIMS reference materials for measuring water in upper mantle minerals. *American Mineralogist*, *102*, 537–547.
Withers, A. C., Hirschmann, M. M., & Tenner, T. J. (2011). The effect of Fe on olivine H_2O storage capacity: Consequences for H2O in the martian mantle. *American Mineralogist*, *96*(7), 1039–1053.
Thompson, S. L., & Lauson, H. S. (1972). *Improvements the CHART D radiation-hydrodynamic code III: Revised analytic equations of state, Sandia National Laboratory Report SC-RR-71 0_+* (p. 113). Albuquerque, New Mexico: Sandia National Laboratory.